Enhanced Bayesian Network with Imprecise Probabilities for Risk Assessment of Concrete Corrosion due to Climate Change

A.Perin[1], S. A. Hosseini[2], E. Zio[2,3], M. Broggi[1], and M. Beer[1,4,5]

[1]*Institute for Risk and Reliability, Leibniz Universität Hannover, Hannover 30167, Germany*

[2]*Energy Department, Politecnico di Milano, Milan 20156, Italy*

[3]*MINES ParisTech, PSL Research University, CRC, Sophia Antipolis 06984, France*

[4]*Department of Civil and Environmental Engineering, University of Liverpool, Liverpool L69 3GH, UK*

[5]*International Joint Research Center for Resilient Infrastructure & International Joint Research Center for Engineering Reliability and Stochastic Mechanics, Tongji University, Shanghai 200092, China*

May 17, 2025

Abstract

The susceptibility of concrete structures to chemical corrosion is significantly influenced by environmental exposure, a condition intensified by climate change. Bayesian Network has demonstrated significant effectiveness in modeling the interdependencies in such corrosion processes. However, traditional Bayesian Networks face challenges in addressing aleatoric and epistemic uncertainties and in accommodating the impacts induced by

Name: Andrea Perin
Date: May 17, 2025
Name: andrea.perin@irz.uni-hannover.de

climate change on corrosion dynamics. We propose an enhanced Bayesian Network framework that aims to effectively manage these uncertainties by leveraging continuous nodes and incorporating imprecise probabilities, especially from climate change projections. This framework is applied to carbonation and chloride corrosion phenomena, which are the main degradation mechanisms in concrete structures, considering the intertwined uncertainties associated with environmental parameters such as temperature, carbon dioxide concentration, and relative humidity over time. The results demonstrate the significant capabilities of the enhanced Bayesian Network framework, not only by improving structural safety analysis to disentangle from the remaining uncertainties but also by advancing the mitigation strategies for corrosion risks in concrete structures.

Keywords— structural reliability analysis, risk assessment, Bayesian networks, enhanced Bayesian networks, imprecise probability, concrete barriers degradation, chemical corrosion, climate change

1 Introduction

Concrete is one of the most fundamental materials in modern infrastructure, which forms the backbone of buildings, bridges, tunnels, and various safety-critical domains, e.g. the offshore industry, nuclear power plants, and nuclear waste repositories. Beyond its strength, durability, and cost-effectiveness, environmental exposure can have an adverse potential to undergo chemical processes that accelerate its degradation [1]. Structures located in coastal or urban areas, where humidity, chlorides, and fluctuating temperatures accelerate deterioration, are especially prone to corrosion-related process [2]. One such process is carbonation, where atmospheric carbon dioxide (CO_2) reacts with calcium compounds by forming calcium carbonate over its useful life, challenging the reinforced concrete structures through the reduction of the alkalinity

of the concrete, that is, lowering the PH, where compromises the protective layer surrounding the embedded steel reinforcement. As carbonation progresses and pH decreases, this protective layer breaks down, leaving steel vulnerable to corrosion [3]. This deterioration can lead to cracks, cracking, and weakening of the bond between the steel and concrete, ultimately diminishing the structural durability. Another degradation mechanism is chloride-induced corrosion, which leads to the accumulation of chloride ions around the embedded steel reinforcement. Unlike carbonation, chloride ions can penetrate even high-alkalinity concrete without necessarily lowering the pH, directly compromising the passive film on steel. Once a critical chloride concentration threshold is reached on the steel surface, localized corrosion begins, often in the form of pitting [4]. In fact, the corrosion risk of concrete structures is essential to take into account for safety-critical applications during long-term periods, e.g., as engineering barriers of radioactive waste repositories [5]. To maintain structural integrity over service life, risk assessment frameworks must incorporate these environmental uncertainties, allowing the development of predictive models and then maintenance strategies [6]. Here, a well-structured risk assessment is supposed to be effective, capable of accounting for multiple scenarios, uncertainties, and the available information.

Traditional risk assessment tools, such as Event Trees (ET) [7] and Fault Trees (FT) [8], are the most widely used for prognostic analysis but are inherently limited by Boolean logic, making them unsuitable for exhaustive dependability analysis. Bayesian Networks (BNs), which model system dependencies through directed acyclic graphs [9], can be seen as generalized FTs. BNs framework can model uncertainties in the behavior of the *and* and *or* gates, express imperfect knowledge on system behavior by incorporating common cause fail-

ures, and consider multistate events, including probabilistic dependencies.

A BN enables diagnostic problem-solving while preserving the multi-scenario analysis and minimal cut-set identification features inherent to FT analysis. Since risk assessment often involves conditional probabilities, BNs provide an efficient factorization of joint probability distributions, making them particularly useful for reliability analysis, as shown by the work of Langseth and Portinale [10]. BNs have been used in several applications, including maintenance planning of structural components [11], multi-hazard fragility assessment of bridges [12, 13], disaggregation of structural failure [14], deterioration processes in engineering structures [15–17], and especially the reliability assessment of reinforced concrete structures [18–20].

Despite their advantages, conventional BNs are limited in their ability to model aleatoric uncertainties, as they primarily rely on expert knowledge and discrete probability assignments, e.g., considering the evolving impact of climate change. Given that the uncertainties in corrosion dynamics are strongly influenced by CO_2 concentration, temperature, and relative humidity, it is essential to incorporate climate change projections into risk analysis tools to ensure more accurate assessments of structural longevity.

To address these limitations, we propose an enhanced Bayesian Network (eBN) with the incorporation of imprecise probabilities aimed at handling both aleatoric and epistemic uncertainties that remained in traditional BN. The eBN framework integrates structural reliability methods, such as First-Order Reliability Methods (FORM), and advanced Monte Carlo techniques into conventional BN structures. The extension allows eBNs to incorporate aleatoric uncertainties by introducing continuous nodes associated with probability distributions, significantly enhancing their applicability to risk assessment; to combine the probabilistic reasoning capabilities with well-established reliability methods; to adopt

imprecise probabilities into the eBN framework, incorporating both epistemic and aleatoric uncertainties into the assessment process; to model complex interactions between environmental variables and material properties over time. Thus, the eBN framework enables the embedding of climate change projections variables, e.g., CO_2 concentrations, temperature, and humidity, into corrosion risk, and allows a scenario-based evaluations of the impact of the environmental conditions over the chemical degradation of concrete in time. With the ability to assess climate change scenarios, eBNs offer a forward-thinking framework, ensuring the resilience of concrete infrastructure in the face of evolving environmental stressors, ultimately enabling risk-informed decision-making for adaptation and mitigation strategies.

The remaining sections of the manuscript are structured as follows: Section 2 formulates the eBN-based framework for risk assessment by incorporating imprecise probabilities, Section 3 describes the case study of the eBN application for two degradation processes of concrete structures, carbonation-induced and chloride-induced corrosions, and Section 4 presents the results. In Section 5, conclusions are drawn.

2 eBN-based Framework for Risk Assessment

The eBN is a directed acyclic graph designed to improve traditional BN modeling by incorporating both discrete and continuous events for a more comprehensive probabilistic analysis. Both eBNs and BNs frameworks, consist of two primary elements: nodes and edges. A node represents an event with its possible determinations and is defined through a Conditional Probability Table (CPT); an edge expresses a direct dependence among 2 nodes, where the originating node is termed the parent. A node with no incoming edges is referred to as a

root node. Nodes that are directly connected by outgoing edges from a given node are called its child nodes. Non-root nodes have a CPT determined by the combination of all their discrete parents' states.

2.1 eBN main features

In a traditional BN, each node represents a discrete random variable that can take on a finite number of mutually exclusive and collectively exhaustive states. For instance, root nodes A and B, as well as node D in the network depicted in Fig. 1a, fall into this category. These nodes are referred to as discrete nodes, and their CPTs are defined using precise probability values, as illustrated in Table 1. The traditional BN framework is extensively discussed in the work of Russell and Pearl [21], while its application to reliability analysis is examined in detail in the study by Langseth and Portinale [10]. The eBN framework is capable of handling continuous nodes, which are nodes associated with continuous random variables and consequently, an infinite number of possible states. The CPT of such nodes is defined using a probability density function (PDF) when the node is a root node, and using a conditional PDF when the node has one or more discrete parents. For instance, node C in Fig. 1a has a CPT characterized by a univariate normal distribution, $Normal(0, 1)$, as illustrated in Table 1.

A node whose CPT is not explicitly defined a priori but instead determined through a model that maps the inputs from its parent nodes to an output generated by the model itself is referred to as a functional node. The functional nodes can be continuous or discrete. In the case of continuous functional nodes, the model alone is sufficient to empirically reconstruct the corresponding CPT. However for discrete functional nodes, a performance function is required to define their two possible states, which typically represent a failure state and a

safe state. For example, node M in Fig. 1a is a discrete functional node that operates based on this performance function.

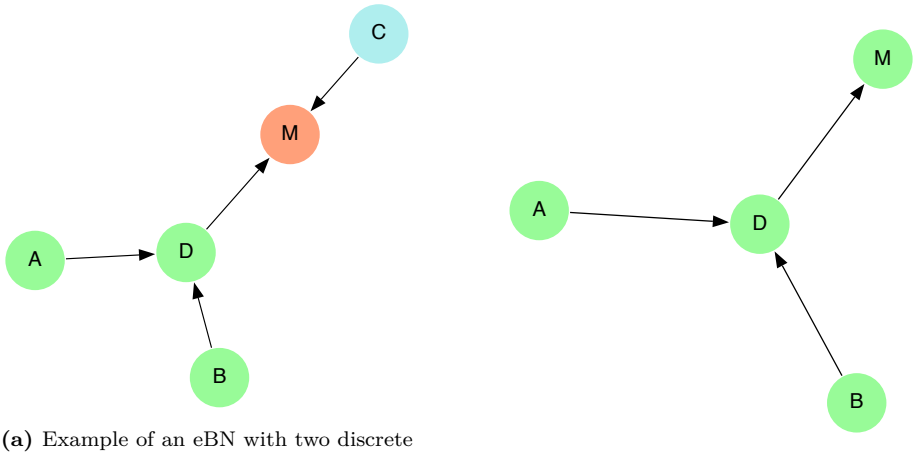

(a) Example of an eBN with two discrete root nodes A and B, one continuous root node C, one discrete non-root node D and one discrete functional node M

(b) Associated rBN where the continuous node C is eliminated and the functional nodes M is evaluated

Figure 1: Example of reduction of an eBN when no continuous node is discretized

Table 1: CPTs of the eBN

Node	**CPT**			
A	a1	a2		
	0.5	0.5		
B	b1	b2		
	0.3	0.7		
C	$Normal(0; 1)$			
D	**scenario**		d1	d2
	a1	b1	0.6	0.4
	a1	b2	0.1	0.9
	a2	b1	0.5	0.5
	a2	b2	0.5	0.5
M	M: $f(d, c) = d - c$ P: $1 - f(d, c) < 0$			

The eBN framework retains the core advantages of traditional BNs, such as the ability to perform multi-scenario analysis, serving as a multidisciplinary aggregator of information, and providing a clear visual representation of complex problems through structured parent-child relationships. EBNs further enhance risk assessment capabilities by incorporating aleatoric uncertainties through the inclusion of continuous nodes. This addition allows for a more robust and realistic representation of uncertain phenomena, thereby improving the model's ability to reflect real-world complexities.

Let $\mathbf{Y} = \{Y_1, \ldots, Y_{n_Y}\}$ represent the collection of discrete nodes in the eBN, where each Y_i is a discrete random variable with k_i possible states $\{y_i^1, \ldots, y_i^{k_i}\}$, and let $\mathbf{X} = \{\mathbf{X}_1, \ldots, \mathbf{X}_{n_X}\}$ denote the collection of continuous nodes, where each $\mathbf{X}_i$ is associated with a set of continuous random variables, $\mathbf{X}_i = \{X_{i,1}, \ldots, X_{i,n_i}\}$. The joint distribution function of the system can then be expressed through the factorization given in Eq. 1. This mathematical formulation, combined with the application of structural reliability methods (SRMs) to compute joint probability measures in networks with continuous parents, is detailed in the work of Straub and Der Kiureghian [22].

$$p(\mathbf{y}|\mathbf{x})f(\mathbf{x}) = \prod_{Y_i \in \mathbf{Y}} p(y_i|Pa(Y_i)) \prod_{X_i \in \mathbf{X}} f(\mathbf{x}_i|Pa(\mathbf{X}_i)) \tag{1}$$

One of the key strengths of BNs is their ability to utilize exact algorithms to perform *inference* based on available *evidence*, meaning the system's probabilities can be updated given any observed value of a node within the network. This feature enables BNs to provide accurate and efficient reasoning about uncertain systems. The continuous nature of these nodes complicates the inference process, as they introduce infinite possible states, making traditional exact-inference algorithms inapplicable. To address this limitation, once the CPTs

for all functional nodes are evaluated, a *node elimination* algorithm, derived from graph theory [23], is employed. This algorithm systematically removes the continuous nodes from the network, while preserving the acyclicity of the eBN at each step, as illustrated in Fig. 1. By applying this algorithm, the eBN is reduced to a standard BN, which is referred to as the *reduced* BN. This reduction allows for the use of well-established exact-inference algorithms for BNs, which enable both prognosis and diagnostic analysis.

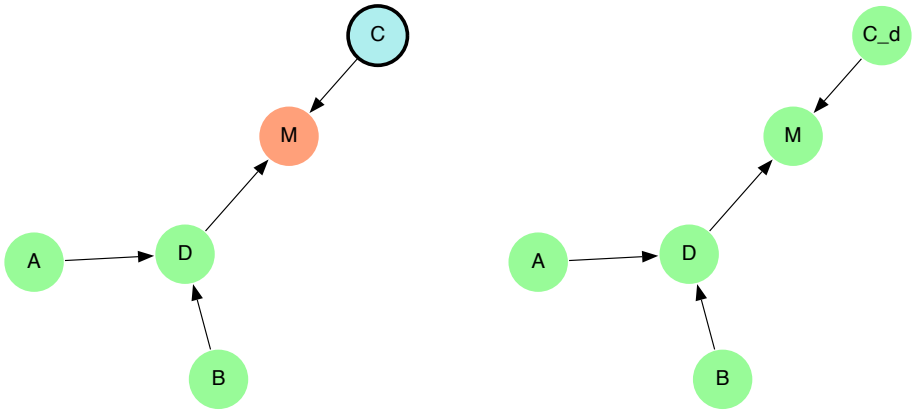

(a) Example of the same eBN of Fig.1a with continuous node C to be discretized

(b) Associated rBN where the continuous node C is discretized into Cd

Figure 2: Example of reduction of an eBN when continuous node is discretized

Table 2: CPT of the discretized node Cd with a $[-3; 0; 3]$ as discretization interval

$[-\infty; -3]$	$[-3; 0]$	$[0; 3]$	$[3; \infty]$
0.0013499	0.49865	0.49865	0.0013499

Once all continuous nodes have been removed from the network during the network reduction phase, both exact and approximated discretization algorithms can be employed to either consider evidence over these nodes or update their CPTs. This is shown in Fig. 2, where the continuous node C is discretized

Table 3: CPT of the node M after being evaluated

scenarios	$Mfail$	$Msafe$
$d1; [-\infty; -3]$	0	1
$d1; [-3; 0]$	0	1
$d1; [0; 3]$	0.48	0.52
$d1; [3; +\infty]$	1	0
$d2; [-\infty; -3]$	0	1
$d2; [-3; 0]$	0	1
$d2; [0; 3]$	0.79	0.21
$d2; [3; +\infty]$	1	0

into the discrete node Cd, with the corresponding CPT shown in Tab. 2. By discretizing the continuous nodes, it becomes possible to incorporate them into the inference process, allowing for the evaluation of conditional probabilities that involve the former continuous nodes. This is illustrated in Tab. 4 for the direct inference problem and in Tab. 5 for the inverse inference problem. Discretization algorithm effectively integrates continuous nodes into the eBN framework, enabling the use of traditional inference techniques while accurately representing aleatoric uncertainty as continuous random variables.

Therefore, eBN integrates classical probabilistic modelling with structural reliability methods to form a robust framework for both prognosis and diagnosis across various engineering domains, enhancing decision-making through a more accurate and realistic representation of uncertainty associated with continuous variables.

Table 4: Direct inference results on node M given node Cd state

evidence	$P(M = fail\|Cd)$	$P(M = safe\|Cd)$
$Cd = [-\infty; -3]$	0	1
$Cd = [-3; 0]$	0	1
$Cd = [0; 3]$	0.99605	0.00395
$Cd = [3; \infty]$	0.00395	0.99605

Table 5: Inverse inference results on node Cd given node M in a failure state

Query	$P(Query\|M = Mfail)$
$Cd = [-\infty; -3]$	0
$Cd = [-3; 0]$	0
$Cd = [0; 3]$	0.68305
$Cd = [3; \infty]$	1

2.2 Imprecise probabilities

In the current eBN framework, only aleatoric uncertainties are explicitly considered, represented by univariate PDFs, while discrete nodes are assigned crisp probability values. However, in real-world applications, both probability distributions and probability assignments often rely on subjective probability, which reflects expert judgments and incomplete or limited data. This reliance on subjective probability arises from different factors, such as the inherent unpredictability of some system parameters or the difficulty in obtaining precise data. To address this challenge, imprecise probability theory provides a robust and flexible mathematical framework [24] for modelling epistemic uncertainties. These uncertainties stem from sources such as conflicting expert opinions, sparse or incomplete datasets, measurement errors, and general knowledge gaps that are common in many engineering and decision-making contexts. An eBN that incorporates imprecise probabilities will be referred to as an imprecise eBN throughout the remainder of this paper, enabling more accurate representations of uncertainty in complex systems.

In the proposed approach, epistemic uncertainties are incorporated into the eBN framework by extending discrete and continuous nodes through imprecise probability theory. For discrete nodes, the traditionally crisp probability values assigned to each possible state are replaced by probability intervals [25], as demonstrated by node D in Fig. 3a. This replacement captures the inherent

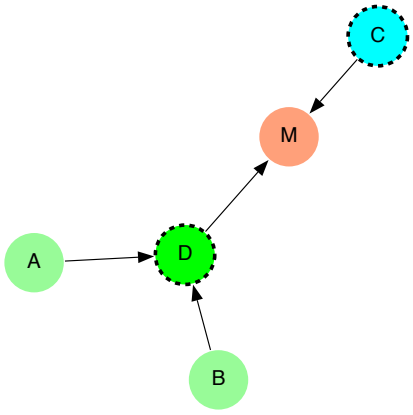

(a) Example of the same eBN of Fig.1a but continuous node C and discrete node D are imprecise

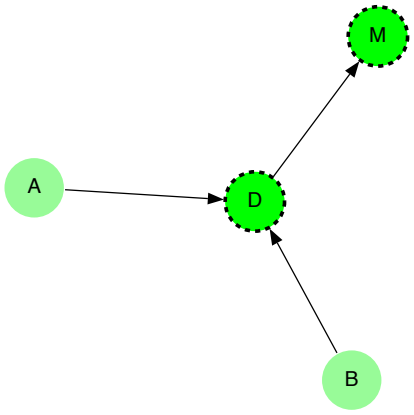

(b) Associated rBN where model node M is imprecise

Figure 3: Example of reduction of eBN with imprecise probabilities

Table 6: CPTs of the eBN with imprecise probabilities

Node	**CPT**		
C	$Pbox\{Normal\}(\mu = [-0.5; 0.5]; \sigma = [0.8; 1.2])$		
D	**scenario**	d1	d2
	a1 b1	$(0.3; 0.5)$	$(0.5; 0.7)$
	a1 b2	$(0.0; 0.2)$	$(0.8; 1.0)$
	a2 b1	$(0.4; 0.6)$	$(0.4; 0.6)$
	a2 b2	$(0.4; 0.6)$	$(0.4; 0.6)$
M	M: $f(d, c) = d - c$ P: $1 - f(d, c) < 0$		

Table 7: CPT of the node M after being evaluated in the imprecise eBN

scenarios	$Mfail$	$Msafe$
$d1$	$(0.02; 0.6)$	$(0.4; 0.98)$
$d2$	$(0.12; 0.76)$	$(0.24; 0.88)$

uncertainty in probability estimation, reflecting situations where precise probability values cannot be determined. Similarly, for continuous nodes, traditional univariate PDFs are generalized into either probability boxes [26] or probability

intervals that refer to the quantity of interest itself, rather than a probability value as seen for discrete nodes. For example, node C in Fig. 3a illustrates this approach, enabling a more flexible representation of uncertainty in continuous distributions.

The presence of imprecise nodes, i.e. nodes with imprecise CPTs, introduces two main consequences for the analysis of the network. First, whenever a continuous node is imprecise, traditional SRMs, such as First Order Reliability Methods (FORM), Monte Carlo simulations, or Advanced Monte Carlo simulations, are no longer directly applicable for evaluating functional nodes. Instead, alternative methods, such as DoubleLoop simulation or Random Slicing [27], must be employed to appropriately handle the imprecision in continuous variables. The presence of imprecise parents for functional nodes means that these nodes are defined by a CPT that includes interval values for both failure and safe state probabilities. In the reduction process shown in Fig. 3 nodes CPTs are presented in Tab. 6 and resulting failure probability interval are the one of Tab. 7. This approach allows for a more flexible and accurate analysis of systems where uncertainty is present, particularly when dealing with imprecise inputs and uncertain model parameters.

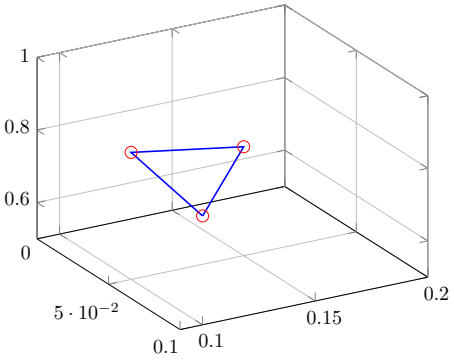

Figure 4: Extreme points of the polytope identified by the CPT in Tab.8

states	**P**
s1	$(0.05; 0.1)$
s2	$(0.1; 0.2)$
s3	$(0.8; 0.9)$

Table 8: CPT of a discrete imprecise node S with 3 states $s1$, $s2$ and $s3$

Whenever a discrete node is imprecise, the rBN is no longer a traditional BN, but instead becomes a Credal Network (CN) [28]. In the context of CNs, standard exact inference algorithms cannot be directly applied, as the presence of imprecision in the node probabilities introduces a more complex structure. To address this, the concept of *strong extension* from the credal set theory [29] is employed. This extension allows the CN to be decomposed into a set of traditional BNs, each corresponding to one of the extreme points of the n-dimensional polytope in the probability space defined by the intervals of the CPTs of the nodes. This process is illustrated in Fig. 4, where each extreme point represents a distinct interpretation of the imprecise probabilities. Consequently, solving the inference problem for the reduced CN (rCN) of an imprecise eBN requires solving multiple inference problemsone for each extreme point. The result of this process is no longer a single crisp probability value but rather a set of probability bounds, reflecting the uncertainty introduced by the imprecision. This is exemplified in Tab. 9, which shows the probability bounds for nodes A and B given that node M is in a failure state. These bounds provide a more flexible and robust representation of uncertainty, offering a range of possible outcomes instead of a single deterministic probability, thereby capturing the effects of imprecise information in the network.

Table 9: Inverse inference results on node A and B given node M in a failure state

Query	$P(Query\|M = Mfail)$
$A = a1$	$(0.281, 0.673)$
$A = a2$	$(0.327, 0.719)$
$B = b1$	$(0.205, 0.435)$
$B = b2$	$(0.565, 0.795)$

The examples previously discussed, along with the case study and results presented in the following sections, have been implemented using the Julia library *EnhancedBayesianNetworks.jl* [30].

3 Case of Study

Concrete degradation is a crucial factor for long-term performance assessment of engineering radioactive waste disposals due to their environmental exposure. Over time, degradation processes such as carbonation can lower the alkalinity of concrete, which is essential for protecting the steel reinforcements within these structures from corrosion. The onset of corrosion can compromise the integrity of containment walls, potentially leading to breaches that could release radioactive contaminants into the environment, and ultimately dose intake. Properly accounting for these degradation pathways in performance assessment of nuclear repositories over climatic projections is essential for ensuring the containment's longevity and, hence, the protection of public health and the environment. To implement an eBN with this purpose, chemical degradation of concrete structures are evaluated over climatic change projections.

3.1 Concrete degradation

The two most critical degradation processes impacting concrete infrastructure in radioactive waste disposal are carbonation-induced corrosion and chloride-induced corrosion. This section provides a concise overview of both phenomena and presents their respective mathematical models.

3.1.1 Carbonation-induced corrosion

The abundance of CO_2 increases the risk of carbonation-induced corrosion in concrete structures [31, 32]. The interaction between concrete and atmospheric CO_2 causes the formation of calcium carbonate, a process known as carbonation, which reduces the concrete's alkalinity and makes the steel reinforcement in the concrete susceptible to corrosion, as presented by Glasser et al. [1]. Carbonation is quantified by measuring the depth from the concrete surface to where the

alkalinity reaches a minimum allowable value. Once carbonation reaches the steel reinforcements, the corrosion propagation phase begins, accelerating the degradation of the concrete structure. In this study, the carbonation depth, denoted as $x_c(t)$, is assessed using the associated model of Stewart et al. [33] and Bastidas-Arteaga et al. [34]. Specifically, Eq.2 describes the increment in carbonation depth Δx_c at time t, relative to the depth reached at time $t - \Delta T$, where ΔT denotes the selected evaluation interval in years, e.g., for a decade, $\Delta T = 10$.

$$\Delta x_c(t, \Delta T) = \sqrt{\frac{2\ k_{site}\ C_{CO_2}(t)\ f_T^C(t)\ f_{RH}^C(t)\ (D_0^C)^{-n_d}}{a}\ \Delta T}\ \cdot\ \left(\frac{1}{\tau(t, \Delta T)}\right)^{n_m} \tag{2}$$

In defining Δx_c, $\tau(t, \Delta T)$ is an integer representing the number of ΔT intervals needed from the reference year to reach the evaluation year t, e.g., $t = 2020$ implies $\tau = 1$, $t = 2030$ implies $\tau = 2$, and so on. The variable k_{site} accounts for potentially higher CO_2 concentration values in industrial and urban areas; C_{CO_2} is the time-dependent CO_2 concentration measured in $\mathrm{kg\,m^{-3}}$ is the CO_2 diffusion coefficient at reference time t_0, measured in $\mathrm{m^2\,s^{-1}}$; n_d is the diffusion coefficient aging factor; and n_m is a factor accounting for exposure to microclimatic wetting and drying cycles, with a value of 0 for sheltered outdoor environments, or 0.12 for unsheltered outdoor.

The time-independent quantity a is derived from Eq.3, where α_h is the degree of hydration, expressed as a function of the water-to-cement ratio w/c. The cement content Ce is measured in $\mathrm{kg\,m^{-3}}$, the calcium oxide fraction in cement CaO is approximately 0.65, and the molar masses of CO_2 and CaO are

$44\,\mathrm{kg\,mol^{-1}}$ and $56\,\mathrm{kg\,mol^{-1}}$, respectively.

$$\begin{cases} a = 0.75\ Ce\ CaO\ \alpha_H \frac{M_{CO_2}}{M_{CaO}} \\ \\ \alpha_h = 1 - e^{-3.38\frac{w}{c}} \end{cases} \tag{3}$$

The time-dependent quantities f_T^C and f_{RH}^C allow the incorporation of climate variable effects, associated with climate change projections, into the carbonation depth evaluation, as presented in the analytical models by Bastidas-Arteaga et al. [35]. Specifically, f_T^C represents the dynamic effect of temperature on carbonation, impacting the diffusion coefficient according to the Arrhenius Law [36], as shown in Eq.4. Here, E is the activation energy of the diffusion process, i.e., $38.3\,\mathrm{kJ\,mol^{-1}}$; R is the gas constant, i.e., $8.314\,\mathrm{kJ\,mol^{-1}\,K^{-1}}$; $T(t_0)$ is the reference temperature, i.e.,$293\,\mathrm{K}$; and $T(t)$ is the temperature in Kelvin at time t.

$$f_T^C(t) = e^{\frac{E}{R}\left[\frac{1}{T_0} - \frac{1}{T(t)}\right]} \tag{4}$$

The effect of relative humidity (RH) has been extensively studied. Research by Al-Khaiat and Fattuhi [37] suggests that RH levels below 30% do not significantly impact carbonation depth, whereas Bary and Sellier [38] indicates that RH levels above 50% have a significant influence. For this study, the analytical model chosen to describe the RH effect over time on the diffusion coefficient is the one proposed by Bastidas-Arteaga et al. [35], detailed in Eq.5.

$$\begin{cases} 0 & if\ RH \leq 0.25 \\ \left[\frac{1-RH(t)^\beta}{1-RH_0^\beta}\right]^\alpha & otherwise \end{cases} \tag{5}$$

Here, RH_0 is the reference value for RH, while α and β are independent parameters of exposure conditions. In this case study, the reference RH is set to 0.65,

α is 5, and β is 2.5.

3.1.2 Chloride-induced corrosion

The penetration and movement of chloride ions into concrete structures involve the electrochemical dissolution of iron, leading to the degradation of concrete barriers. Chloride ingress into concrete is typically described using a diffusion model, which is a single mass transport equation for chloride ion transport. In this study, a time-dependent model is applied, incorporating the chloride diffusion coefficient to estimate chloride concentration over time. The chloride concentration at a depth z and time t is described by Eq. 6.

$$C(z,t) = C_0^{Cl}\left[1 - erf\left(\frac{z}{2\sqrt{k_e\ k_t\ k_c\ f_T^{Cl}(t)\ f_{RH}^{Cl}(t)\ D_0^{Cl}\ \omega\ \tau(t,\Delta T)}}\right)\right] \quad (6)$$

Here, C_0^{Cl} represents the chloride concentration at the boundary; for atmospheric areas remote from coasts, C_0^{Cl} is typically around $1.15\,\mathrm{kg\,m^{-3}}$, whereas, in coastal or tidal areas, the chloride concentration at the surface is significantly higher. D_0^{Cl} is the reference chloride diffusion coefficient; k_e is the environmental coefficient; k_t is the test method factor, and k_c is the curing factor. Coefficient ω represents the number of seconds in 10 years while $\tau(t,\Delta T)$ has the same definition given in Sec. 3.1.1.

Similar to carbonation, there are two time-dependent quantities that account for the effects of climate change projections on temperature and relative humidity: f_T^{Cl} and f_{RH}^{Cl}.

$$f_{RH}^{Cl}(t) = \left[1 + \frac{(1 - RH(t))^4}{(1 - RH_0)^4}\right]^{-1} \quad (7)$$

The temperature effect is consistent with that defined for carbonation in Eq.4, thus $f_T^C = f_T^{Cl}$. The effect of RH is expressed in the work of El Hassan et al. [39] as shown in Eq.7.

3.2 eBN for concrete degradation

The eBN framework is exemplified to perform risk analysis for concrete degradation over climatic change prjections. Climate change data are taken from the catalogue provided in Copernicus Climate Change Service [40] and includes three main projection scenarios referred to three different shared socioeconomic pathway (*ssp*), namely *ssp1*, *ssp2*, and *ssp5*. These projections account for variations in temperature, CO_2 concentration, and relative humidity from 2020 to 2100, relevant for concrete corrosion models.

In this study the eBN integrates the two degradation models presented in 3.1.1, and in 3.1.2 and is structured to capture the probabilistic dependencies considering epistemic and aleatoric uncertainties, between climate conditions of temperature, relative humidity, and CO_2 concentration, material properties, e.g. diffusion coefficients, water-to-cement ratio, and the final state of the system, through the carbonation and chloride effect on concrete. The following sections details the eBN structure, the probabilistic modelling of input variables, and its application to the case study of a radioactive waste disposal concrete degradation. Initially, the carbonation-induced and chloride-induced corrosion models are examined separately to enhance clarity and comprehensibility. Subsequently, the complete eBN framework, integrating both degradation mechanisms, is presented.

3.2.1 eBN – Carbonation-induced corrosion model

The eBN representing the carbonation process, illustrated in Fig. 5, includes two primary discrete root nodes. The first is the node t, which denotes the selected time slice (considering ΔT equals to a decade); it consists of nine equally probable states, corresponding to the decades from 2020 to 2100. The second node, *proj*, represents the climate change projections, with three equally likely

states, each associated with an *ssp* (i.e *ssp1*, *ssp2* and *ssp5*).

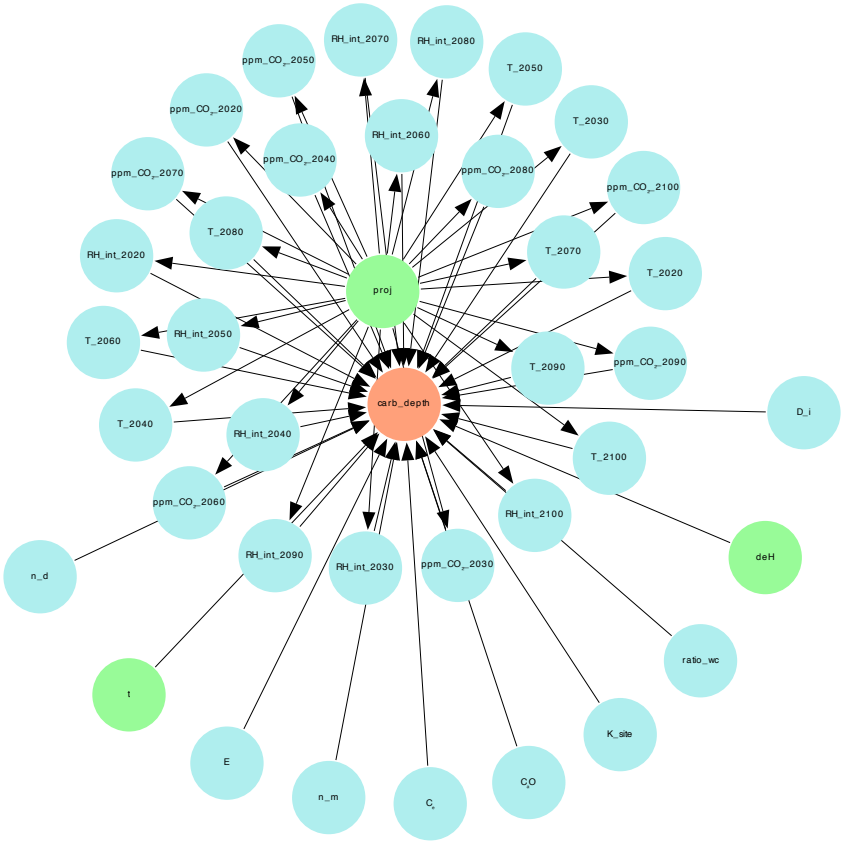

Figure 5: Carbonation-induced corrosion eBN with precise nodes

A third discrete root node, *DeH*, is also shown in Fig. 5. This node represents a control variable to reduce the RH below a threshold. Specifically, whenever RH exceeds 0.25, the node enforces a reduction to 0.2. These values were selected based on the influence of RH on the carbonation model, as illustrated in Fig. 6.

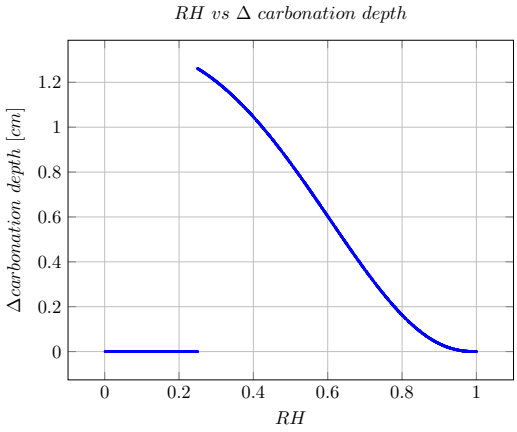

Figure 6: RH effect on carbonation depth

The DeH node is modelled as a Boolean variable with two states: failed ($P_F = 10^{-4}$) and working ($P_W = 1 - 10^{-4}$).

In addition, eight continuous root nodes are introduced to account for aleatoric uncertainties in the parameters n_d, n_m, E, k_{site}, water-to-cement ratio (w/c), C_e, CaO, and D_0^C. Their CPTs are provided in Table 10. The carbonation

Table 10: Distribution of the continuous root nodes of the eBN depicted in Fig.5

Quantity	Node Name	Distribution
n_d	n_d	$Trunc(N(0.24; 2.88e^{-2}); 0, \infty)$
n_m	n_m	$Trunc(N(0.12; 1.2e^{-2}); 0, \infty)$
E	E	$Uniform(34.853; 41.747)$
k_{site}	k_site	$Trunc(N(1.15; 1.15e^{-2}); 0, \infty)$
w/c	$ratio\_w/c$	$Trunc(LogN(-0.69; 0.05); 0, 1)$
Ce	C_e	$Trunc(N(300; 30); 0, \infty)$
CaO	C_aO	$Uniform(0.585; 0.715)$
D_0^C	D_i	$Trunc(N(2.2e^{-4}; 1.5e^{-5}); 0, \infty)$

process is governed by the model presented in Eq. 2, which explicitly depends on temperature, CO_2 concentration, and RH. These variables are characterized through climate change projections data for a nuclear waste disposal located in Belgium (see Appendix A).

The model is dynamic in nature, as its output corresponds to the increment in carbonation depth accumulated over the decade ending in the year under consideration. Therefore, to evaluate the total carbonation depth, one must consider the cumulative sum of increments from all preceding decades. We have introduced decade-specific nodes for temperature, CO_2 concentration (in ppm), and relative humidity over decades. Examples include T_2020, T_2030, and so on up to T_2100, as shown in Fig. 5. These nodes are all modelled as children of the *proj* node, with distributions detailed in Tables 16, 17, and 18. This structure supports the definition of the functional node *carb_depth*, which is a child of all temperature, CO_2, and RH nodes, as well as of *proj*, *DeH*, and the time slice node *t*. For each time slice, a dedicated model computes the incremental carbonation depth by summing contributions from previous decades. If the resulting total exceeds the threshold of 3 cm, defined by Bastidas-Arteaga et al. [35], the system transitions to a failure state. In the carbonation model, the inputs from the $ratio\_w/c$ node and all the RH percentage change nodes are modified before being passed to the computational component. Specifically, the $ratio\_w/c$ samples are scaled by a factor of 0.1 and then shifted by +0.5, while the RH percentage change samples are randomly assigned as either positive or negative deviations from the reference RH.

3.2.2 eBN – Chloride-induced corrosion model

The chloride-induced corrosion process is represented by the eBN depicted in Fig. 7. This model includes some of the same continuous nodes as the corrosion process eBN, specifically for temperature, CO_2 concentration, RH. It also shares the discrete nodes *proj*, *t* and *DeH*. The effect of relative humidity on the chloride penetration is shown in Fig. 8

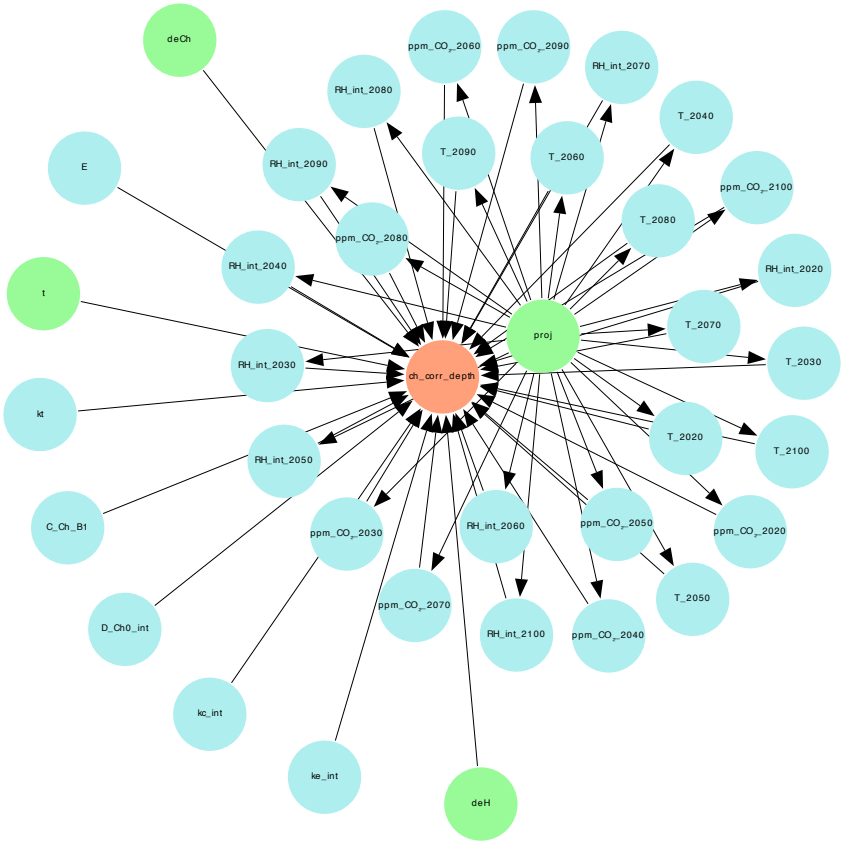

Figure 7: Chloride-induced corrosion eBN with precise nodes

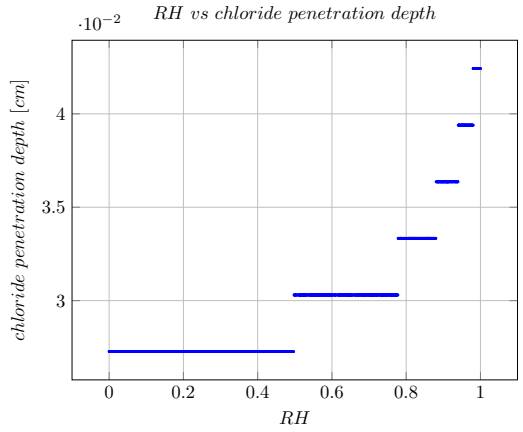

Figure 8: RH effect on chloride penetration depth

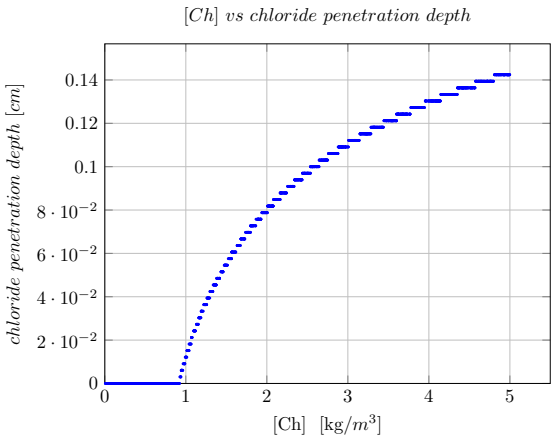

Figure 9: Chloride concentration at system boundary effect on chloride penetration depth

DeCh is a discrete root node that represents a chloride mitigation control variable that reduces the boundary chloride concentration, C_0^{Cl}, when it exceeds a critical level. The effect of the boundary chloride concentration on the model is shown in Fig. 9. *DeCh* node is modelled as a Boolean variable with states *working* and *failed*, with assigned probabilities $P_W = 1 - 10^{-4}$ and $P_F = 10^{-4}$, respectively. It is designed to lower C_0^{Cl} from values above 0.9 to 0.7.

Five continuous root nodes are also included to represent aleatoric uncertainties in the parameters k_t, k_c, k_e, C_0^{Cl}, and the reference diffusion coefficient D_0^{Cl}. Their distributions are detailed in Table 11.

Table 11: Continuous root node distribution of the eBN in Fig.7

Quantity	**Node Name**	**Distribution**
k_t	*kt_int*	$Trunc(N(0.832; 2.4e^{-2}); 0, \infty)$
k_e	*ke_int*	$Gamma(2; 1)$
k_c	*kc_int*	$Beta(2; 2)$
C_0^{Cl}	*C_Ch_B1*	$Trunc(N(1.15; 0.675); 0, \infty)$ [33]
D_0^{Cl}	*D_Ch0_int*	$Trunc(LogN(0; 0.5); 0, 1)$

As with the *ratio_w/c* node and RH percentage change nodes in 3.2.1, the outputs of *ke_int*, *kc_int*, and *D_Ch0_int* are transformed before use in the computational model. Specifically: - *ke_int* samples are scaled by 0.155 and shifted by +0.924; - *kc_int* samples are scaled by 0.7 and shifted by +2.4; - *D_Ch0_int* samples are scaled by 0.2, shifted by +1, and multiplied by 6×10^{-12}.

All these nodes feed into the *ch_corr_depth* node, which uses the model in Eq. 6 to evaluate the chloride concentration $C(z; t)$ across the concrete depth. Unlike the carbonation model, this model is not time-recursive but spatially dependent in the z-direction. The chloride penetration depth is defined as the depth at which $C(z; t)$ first reaches $0.9\,\mathrm{kg\,m^{-3}}$ following the ideas of Francesco et al. [41]. This depth is compared against a failure threshold of 12 cm to assess structural safety. Further implementation details of the *ch_corr_depth* node can be found in the associated code repository.

3.2.3 eBN – Concrete corrosion risk

The final eBN embeds two corrosions models as depicted in Fig. 10. Nodes associated to temperature, CO_2 concentration and RH are shared, as well as the *proj*, *DeH* and t nodes.

Figure 10: Concrete corrosion risk eBN with precise nodes

The functional nodes *ch_corr_depth* and *carb_depth* are initially defined through the set of continuous random variables coming from their continuous parents, the set of discrete random variables coming from their discrete parents, and a simulation technique, selected to be a standard Monte Carlo with 10^4 samples for both of them. The union of these two sets of inputs together with the chosen simulation technique and two performance functions allows solving the structural reliability problems. In this way is possible to obtain the two CPTs associated with the two discrete nodes *ch_corr_depth* and *carb_depth* in the reduced BN of Fig. 11.

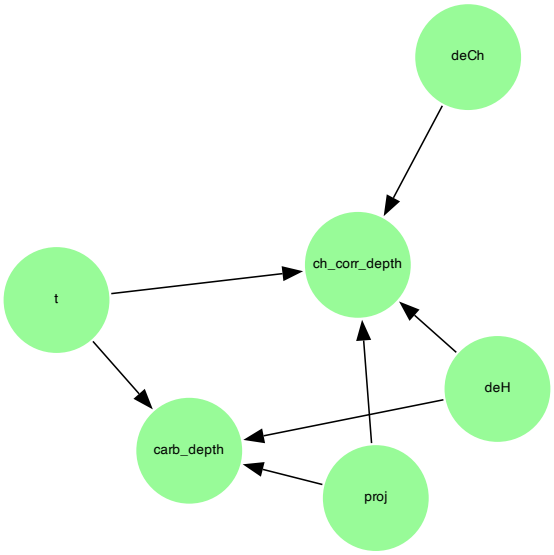

Figure 11: Concrete corrosion risk rBN with precise nodes

In this BN only discrete nodes are present. Both *ch_corr_depth* and *carb_depth* have as parents the discrete nodes referred to the specific time slice, to the specific climatic projection, and the auxiliary discrete node *deH*. The node *deCh* influences the sole node chloride induced corrosion process, therefore it is not a parent of *carb_depth*.

3.2.4 Imprecise eBN – Imprecision in climatic change data

In the climatic change data catalogue [40] each *ssp* come from different downscaled regional climatic model (RCMs). The Gaussian distributions defined in the tables Tab. 16, 17, and 18 have been extrapolated based on limited number of RCMs. A more robust way for dealing with the epistemic uncertainty problem of future projections is represented by the interval probability theory. Therefore, without introducing any hypothesis over the specific distribution for the quantities of interest, have treated as an interval defined only by an upper bound and a lower bound given respectively by the maximum and minimum value of all the simulations related to a specific *ssp*.

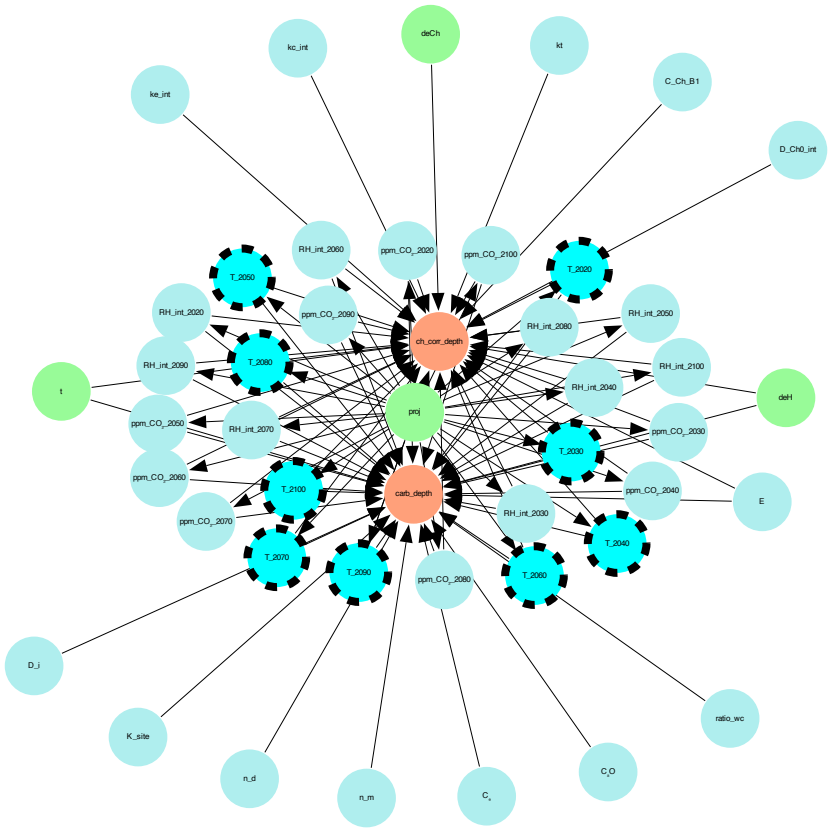

Figure 12: Concrete corrosion risk eBN with imprecise temperature nodes

This concept has been applied to temperature projection obtaining the new node presented in Fig. 12 and defined in Tab. 19. The reduced BN of this imprecise eBN is the Credal Network presented in Fig. 13.

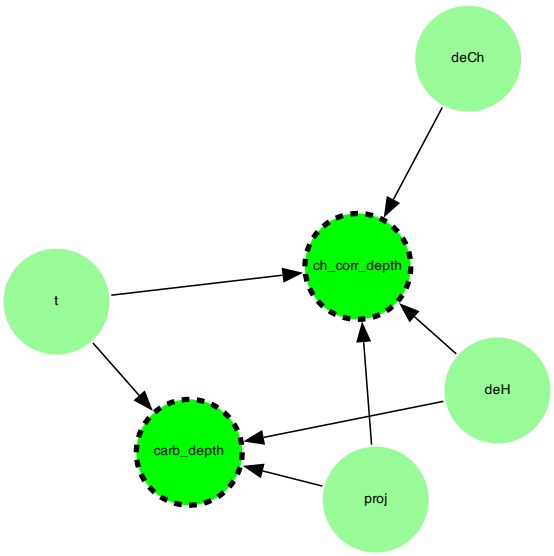

Figure 13: Concrete corrosion risk rBN with imprecise nodes

4 Results & Discussions

This section presents a comprehensive discussion of the results obtained from the application of the eBN framework in addressing uncertainties associated with concrete corrosion risk, with a particular focus on imprecise data arising from climate change projections. Before delving into these findings, we first summarize the outcomes of the sensitivity analysis (SA) conducted on carbonation-induced and chloride-induced corrosion processes.

4.1 Sensitivity Analysis of concrete corrosion processes

SA have been employed to identify the most influential factors affecting concrete corrosion processes. SA is vital for the efficiency of a probabilistic risk assessment tool, as it enables the exclusion of variables with minimal impact on outcomes, thereby reducing the computational demands of the risk assessment

framework. Sobol' indices are widely recognized as one of the most robust and reliable methods for global SA. This is attributed to their rigorous theoretical foundation in variance-based decomposition, their ability to capture both linear and nonlinear dependenciesincluding high-order interactions among random variablesand their clear interpretability [42]. For these reasons Sobol' indices have been evaluated for both corrosion models to rank the effect of the random variables on the outputs.

4.1.1 Carbonation-induced corrosion

The random variables considered in the SA of the carbonation model are the same as those introduced in Sec. 3.2.2. While the variables *Ce*, *Ca*, *k_site*, *n_d*, *n_m*, *E*, *ratio_wc*, and *D_i* follow the same probability distribution across all decades and climatic projections, the distributions of *T*, *ppm_CO₂*, and *RH_int* vary depending on the decade and climate projection.

Figure 14 shows the Sobol' indices for the carbonation model during the first decade under the *ssp1* climate scenario. Both the first-order and total-effect Sobol' indices are negligible for all input variables except for relative humidity, indicating that *RH_int* is the only variable that significantly contributes to the output varianceboth independently (first-order effect) and through interactions with other variables (total effect). Sobol' indices have been computed for each decade and for all considered climate projections. The results consistently exhibit the same trend as illustrated for the first-decade and *ssp1* projection, with relative humidity remaining the dominant factor influencing output variance.

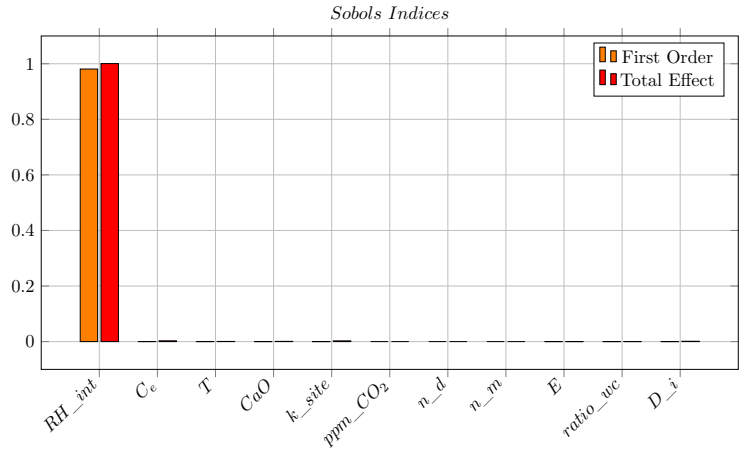

Figure 14: Sobol' indices of the model for carbonation induced corrosion considering the random variables identified by the year 2020 and the projection *ssp1*

In Fig. 15, Sobol' indices are presented under the assumption that all input variables follow uniform probability distributions. For the variables *Ce*, *Ca*, *k_site*, *n_d*, *n_m*, *E*, *ratio_wc*, and *D_i*, the uniform distribution bounds were defined as the minimum and maximum values obtained from 10^4 samples drawn from their respective original distributions. For the time-dependent variables *T*, *ppm_CO₂*, and *RH_int*, the uniform bounds for each decade were derived from the minimum and maximum of a merged set of 3×10^4 samples, aggregated across all climate change projections. This approach is adopted to enhance the potential influence of the distribution tails, particularly those of the original Gaussian distributions, thereby allowing a more comprehensive assessment of the input variables' impact on model output variability. The analysis confirms that relative humidity continues to exert the most significant influence on the variability of the model output, even under the assumption of uniformly distributed inputs.

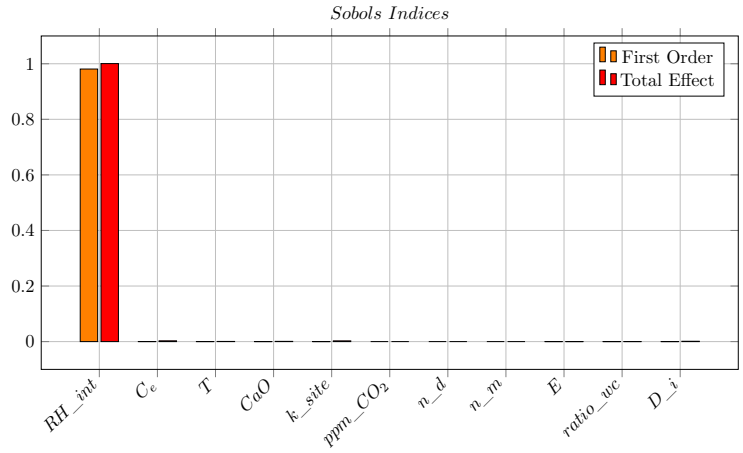

Figure 15: Sobol' indices of the model for carbonation induced corrosion at year 2020 under the uniform distributions assumption

4.1.2 Carbonation-induced corrosion

The same procedure presented in Sec. 4.1.1 have been applied to the chloride-induced corrosion model, obtaining the results presented in Fig. 16 and Fig. 17.

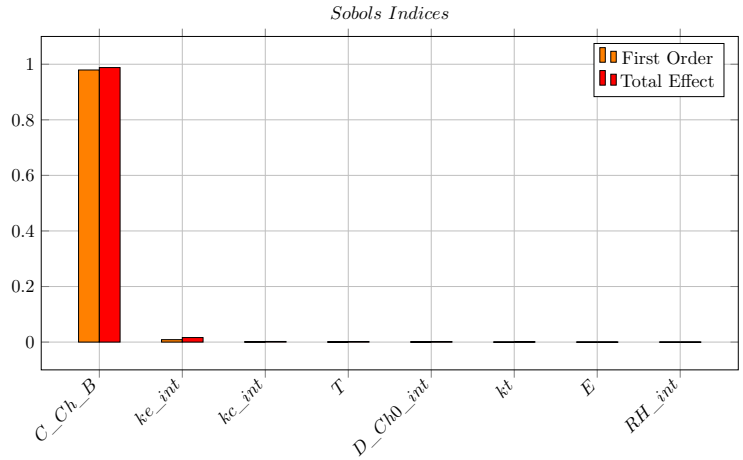

Figure 16: Sobol' indices of the model for chloride induced corrosion considering the random variables identified by the year 2020 and the projection *ssp1*

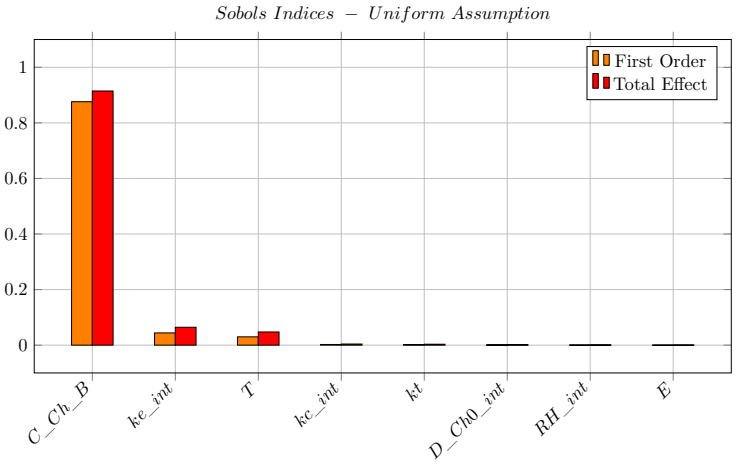

Figure 17: Sobol' indices of the model for chloride induced corrosion at year 2020 under the uniform distributions assumption

For the chloride-induced corrosion model, relative humidity is identified as the primary driver of output variability in both distributional scenarios. However, under the uniform input assumption, additional factors such as temperature, the curing factor, and the environmental factor also exhibit a non-negligible influence on the output variance.

4.2 Exceedance Probabilities for Corrosion

The results of the SA motivated the introduction of two control nodes, *DeH* and *DeCh*, to regulate relative humidity and chloride concentration at the system boundaries. These nodes are defined as follows. The node *DeH* represents a dehumidifier unit, modelled as a root node with a failure probability of 10^{-4}, and is parent to both the model nodes. Its influence is identical across the two models: when operational (i.e., not in a failed state) and when the relative humidity exceeds a specified threshold, it reduces the humidity to a defined target level. In the eBN described in Sec. 3, the threshold and target relative humidity values are set to 0.25 and 0.2, respectively. The node *DeCh* is conceptually

similar to *DeH*. It is also a root node with a failure probability of 10^{-4} and is defined by a threshold and target value for chloride concentration. Unlike *DeH*, *DeCh* influences only the chloride-induced corrosion model, where it acts to reduce the chloride concentration at the system boundary when the threshold is exceeded. In the eBN presented in Sec. 3, the threshold and target chloride concentration values are 0.9 and 0.7, respectively.

4.2.1 Precise eBN

Exceedance probabilities for corrosion are contained in the CPTs of the two functional of the eBNs presented in Sec.3. Results for the precise eBN depicted in Fig. 10 are obtained through Monte Carlo simulation with 10^4 samples and considering a maximum allowed carbonation depth of 3 cm and a maximum allowed chloride penetration of 12 cm, where the chloride penetration is defined as depth where chloride concentration is bigger than $0.9\,\mathrm{kg\,m^{-3}}$, for defining the performance functions of nodes *carb_depth* and *ch_corr_depth*. In particular the CPT of the carbonation node in the precise rBN depicted in Fig.11 has 54 possible scenarios, identified by 9 decades, 3 projections and 2 possible states of the dehumidifier unit. This CPT shows that whenever the dehumidifier unit is working the carbonation process never reaches the failure threshold, for all the decades before year 2060 the failure never happen, and after year 2060 failure of the system can take place with the probabilities shown in table Tab. 12.

Table 12: Carbonation induced corrosion node partial CPT for the precise eBN of Fig. 5

scenarios			states probabilities	
t	**DeH**	**proj**	**failed**	**safe**
2060	broken	ssp1	0.0001	0.9999
2060	broken	ssp2	0.0012	0.9988
2060	broken	ssp5	0.0103	0.9897
2070	broken	ssp1	0.0056	0.9944
2070	broken	ssp2	0.0241	0.9759
2070	broken	ssp5	0.0991	0.9009
2080	broken	ssp1	0.0374	0.9626
2080	broken	ssp2	0.1110	0.8890
2080	broken	ssp5	0.3082	0.6918
2090	broken	ssp1	0.1232	0.8768
2090	broken	ssp2	0.2694	0.7306
2090	broken	ssp5	0.5290	0.4710
2100	broken	ssp1	0.2570	0.7430
2100	broken	ssp2	0.4630	0.5370
2100	broken	ssp5	0.7075	0.2925

The CPT of the chloride induced corrosion node in the precise rBN depicted in Fig.11 has 108 possible scenarios, identified by 9 decades, 3 projections, 2 possible states of the dehumidifier unit and 2 possible states for node *DeCh*. This CPT shows that whenever the unit to reduce the chloride concentration at system boundary is working the chloride induced corrosion process never reaches the failure threshold. Some of the remaining scenarios are shown in table Tab. 13.

Table 13: Carbonation induced corrosion node partial CPT for the precise eBN of Fig. 5

scenarios				states probabilities	
t	**DeH**	**DeCh**	**proj**	**failed**	**safe**
2020	broken	broken	ssp1	0.0045	0.9955
2020	broken	broken	ssp2	0.0054	0.9945
2020	broken	broken	ssp5	0.0043	0.9957
2020	working	broken	ssp1	0.0021	0.9979
2020	working	broken	ssp2	0.0016	0.9984
2020	working	broken	ssp5	0.0021	0.9979
2030	broken	broken	ssp1	0.0462	0.9538
2030	broken	broken	ssp2	0.0445	0.9555
2030	broken	broken	ssp5	0.0470	0.9530
2030	working	broken	ssp1	0.0291	0.9709
2030	working	broken	ssp2	0.0279	0.9721
2030	working	broken	ssp5	0.0301	0.9699
2040	broken	broken	ssp1	0.1159	0.8841
2040	broken	broken	ssp2	0.1179	0.8821
2040	broken	broken	ssp5	0.1266	0.8734
2040	working	broken	ssp1	0.0862	0.9138
2040	working	broken	ssp2	0.0911	0.9089
2040	working	broken	ssp5	0.0975	0.9025
...	...	...	...	...	...
2090	broken	broken	ssp1	0.3361	0.6639
2090	broken	broken	ssp2	0.3711	0.6289
2090	broken	broken	ssp5	0.3884	0.6116
2090	working	broken	ssp1	0.3052	0.6948
2090	working	broken	ssp2	0.3314	0.6686
2090	working	broken	ssp5	0.3577	0.6423
2100	broken	broken	ssp1	0.3510	0.6490
2100	broken	broken	ssp2	0.3771	0.6229
2100	broken	broken	ssp5	0.4194	0.5806
2100	working	broken	ssp1	0.3250	0.6750
2100	working	broken	ssp2	0.3616	0.6384
2100	working	broken	ssp5	0.3828	0.6172

4.2.2 Imprecise eBN

Results for the imprecise eBN depicted in Fig. 12 are obtained through standard Double Loop simulation with an inner Monte Carlo simulation with 10^3 samples.

Performance functions of the two corrosion model nodes are defined in the same way as for the precise ebn. The CPT of the carbonation node in the imprecise rBN depicted in Fig.13 still has 54 possible scenarios, still never reaches the failure threshold whenever the dehumidifier unit is working the carbonation process and for all the decades before year 2050. Failure probability interval after year 2050 are shown in table Tab. 14.

Table 14: Carbonation induced corrosion node partial CPT for the precise eBN of Fig. 5

scenarios			**states probabilities**	
t	**DeH**	**proj**	**failed**	**safe**
2050	broken	ssp1	$[0.0; 0.0]$	$[1.0; 1.0]$
2050	broken	ssp2	$[0.0; 4.76e^{-4}]$	$[0.999524; 1.0]$
2050	broken	ssp5	$[0.0; 0.001]$	$[0.999; 1.0]$
2060	broken	ssp1	$[1.73e^{-6}; 0.002]$	$[0.998; 0.999998]$
2060	broken	ssp2	$[2.50e^{-4}; 0.007]$	$[0.993; 0.99975]$
2060	broken	ssp5	$[0.0; 0.037]$	$[0.963; 1.0]$
2070	broken	ssp1	$[0.0; 0.027]$	$[0.973; 1.0]$
2070	broken	ssp2	$[0.001; 0.073]$	$[0.927; 0.999]$
2070	broken	ssp5	$[0.033; 0.195]$	$[0.805; 0.967]$
2080	broken	ssp1	$[0.005; 0.081]$	$[0.919; 0.995]$
2080	broken	ssp2	$[0.034; 0.212]$	$[0.788; 0.966]$
2080	broken	ssp5	$[0.183; 0.407]$	$[0.593; 0.817]$
2090	broken	ssp1	$[0.036; 0.249]$	$[0.751; 0.964]$
2090	broken	ssp2	$[0.137; 0.369]$	$[0.631; 0.863]$
2090	broken	ssp5	$[0.384; 0.601]$	$[0.399; 0.616]$
2100	broken	ssp1	$[0.157; 0.426]$	$[0.574; 0.843]$
2100	broken	ssp2	$[0.285; 0.614]$	$[0.386; 0.715]$
2100	broken	ssp5	$[0.575; 0.745]$	$[0.255; 0.425]$

As for the precise BN, the CPT of the chloride induced corrosion node in the precise rBN depicted in Fig.13 has 108 possible scenarios and whenever the unit to reduce the chloride concentration at system boundary is working the chloride induced corrosion process never reaches the failure threshold. Some of the remaining scenarios are shown in table Tab. 15.

Table 15: Carbonation induced corrosion node partial CPT for the precise eBN of Fig. 5

scenarios				states probabilities	
t	**DeH**	**DeCh**	**proj**	**failed**	**safe**
2020	broken	broken	ssp1	$[0.0, 0.018]$	$[0.982, 1.0]$
2020	broken	broken	ssp2	$[0.0, 0.02]$	$[0.98, 1.0]$
2020	broken	broken	ssp5	$[0.0, 0.024]$	$[0.976, 1.0]$
2020	working	broken	ssp1	$[6.17e^{-5}, 0.01]$	$[0.99, 0.9993]$
2020	working	broken	ssp2	$[0.000437, 0.015]$	$[0.985, 0.999563]$
2020	working	broken	ssp5	$[4.55e^{-5}, 0.012]$	$[0.988, 0.99995]$
2030	broken	broken	ssp1	$[0.016, 0.099]$	$[0.901, 0.984]$
2030	broken	broken	ssp2	$[0.015, 0.098]$	$[0.902, 0.985]$
2030	broken	broken	ssp5	$[0.0140, 0.094]$	$[0.906, 0.9860]$
2030	working	broken	ssp1	$[0.008, 0.072]$	$[0.928, 0.992]$
2030	working	broken	ssp2	$[0.003, 0.068]$	$[0.932, 0.997]$
2030	working	broken	ssp5	$[0.004, 0.07]$	$[0.93, 0.996]$
2040	broken	broken	ssp1	$[0.0640, 0.165]$	$[0.835, 0.936]$
2040	broken	broken	ssp2	$[0.058, 0.192]$	$[0.808, 0.942]$
2040	broken	broken	ssp5	$[0.064, 0.193]$	$[0.807, 0.936]$
2040	working	broken	ssp1	$[0.041, 0.106]$	$[0.894, 0.959]$
2040	working	broken	ssp2	$[0.042, 0.16]$	$[0.84, 0.958]$
2040	working	broken	ssp5	$[0.036, 0.113]$	$[0.887, 0.964]$
...	...	...	...	...	...
2090	broken	broken	ssp1	$[0.261, 0.442]$	$[0.558, 0.739]$
2090	broken	broken	ssp2	$[0.272, 0.426]$	$[0.574, 0.728]$
2090	broken	broken	ssp5	$[0.319, 0.45]$	$[0.55, 0.681]$
2090	working	broken	ssp1	$[0.231, 0.404]$	$[0.596, 0.769]$
2090	working	broken	ssp2	$[0.247, 0.388856]$	$[0.611144, 0.753]$
2090	working	broken	ssp5	$[0.272, 0.423]$	$[0.577, 0.728]$
2100	broken	broken	ssp1	$[0.286, 0.403]$	$[0.597, 0.714]$
2100	broken	broken	ssp2	$[0.299, 0.425845]$	$[0.574155, 0.701]$
2100	broken	broken	ssp5	$[0.354, 0.495]$	$[0.505, 0.646]$
2100	working	broken	ssp1	$[0.258, 0.391]$	$[0.609, 0.742]$
2100	working	broken	ssp2	$[0.276, 0.404]$	$[0.596, 0.724]$
2100	working	broken	ssp5	$[0.303, 0.46]$	$[0.54, 0.697]$

4.2.3 Results comparison

In this section results regarding the thresholds exceedance probability for the two nodes related to carbonation-induced and chloride-induced corrosion, and

coming from the precise and the imprecise eBN are compared. In particular, as expected is possible to see that in all the analysed cases of Fig. 18, 19 and 20, failure probability intervals always contain the crisp failure probability values coming from the precise eBN.

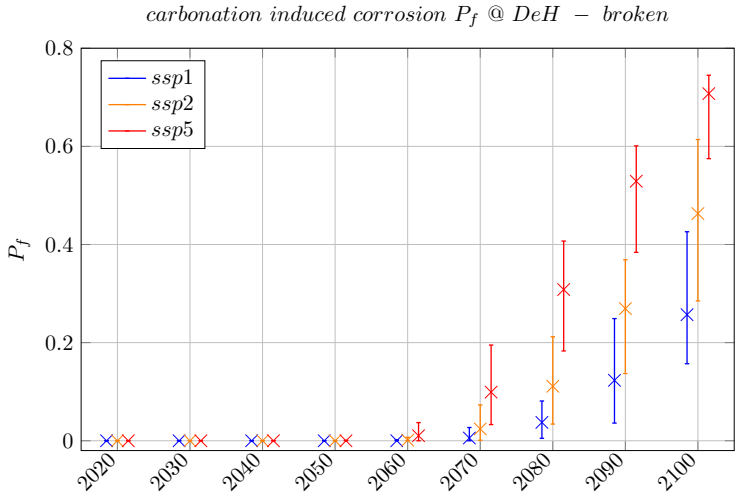

Figure 18: Exceedance probabilities comparison between precise and imprecise eBN for carbonation node and scenarios when the *DeH* is broken

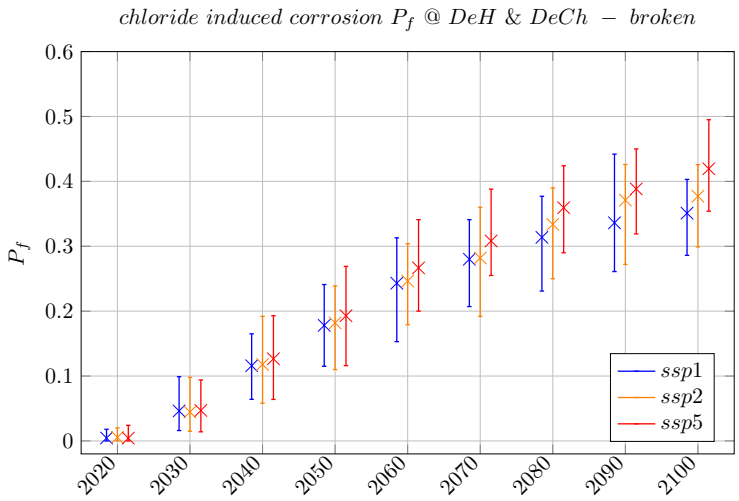

Figure 19: Exceedance probabilities comparison between precise and imprecise eBN for chloride induced corrosion node and scenarios when both *DeH* and *DeCh* are broken

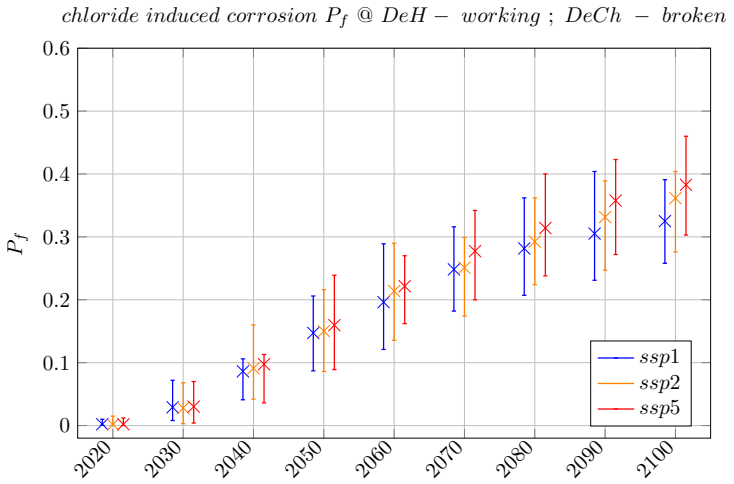

Figure 20: Exceedance probabilities comparison between precise and imprecise eBN for chloride induced corrosion node and scenarios when *DeH* is working and *DeCh* is broken

5 Conclusions

In this work, we employed the framework of imprecise eBN, to tackle the challenge of concrete corrosion under epistemic and aleatoric uncertainties, primarily stemming from climatic change projections. Specifically, we demonstrated its application in the context of radioactive waste disposal, with a focus on concrete integrity as the primary factor influencing reliability of the long-term repository. Concrete chemical degradation has been evaluated using two corrosion models, carbonation-induced and chloride-induced corrosion, showing internally coherent results where the precise failure probabilities consistently fell within the bounds defined by the imprecise intervals.

The adoption of imprecise eBNs enabled aggregation of scenario-based results within a framework that supports exact-inference algorithms to perform diagnostic and prognostic analysis, facilitating and informing the decision-making routine. Furthermore, the framework helps address epistemic uncertainties due

to sparse or incomplete data through the use of imprecise probabilities.

Despite its advantages, the eBN framework presents certain limitations on the computational side. Precise eBN relies on Monte Carlo simulations for functional node evaluation, which leads to high computational costs. This computational burden is even more exacerbated in the imprecise case due to the need for nested simulations and global optimization, as seen in the Double Loop Monte Carlo and Random Slicing methods.

Future developments should consider incorporating additional degradation phenomena to enrich the risk assessment scope. A unified modelling node for the combined effects of carbonation and chloride-induced corrosion should also be explored, avoiding oversimplified strategies such as logical *OR-gate* or additive approaches, which respectively under- or overestimate the risks. Moreover, optimization of control nodes for parameters like chloride concentration and relative humidity should be undertaken with respect to operational costs and performance. Finally, alternative approximate inference strategies, such as Non Intrusive Stochastic Simulation (NISS) [43] and Collaborative and Adaptive Bayesian Optimization (CABO) [44], merit investigation to alleviate the computational demands of the imprecise eBN framework.

A Appendix

To simulate long-term climate behaviour, a range of Global Climate Models (GCMs) is utilized to represent large-scale environmental dynamics. For regional-scale applications, these coarse-resolution outputs are refined through down-scaling techniques using Regional Climate Models (RCMs). Climate projections for Belgium, based on *ssp* scenarios, are derived from the Coupled Model Intercomparison Project Phase 6 (CMIP6), which aggregates output from multiple GCMs and RCMs [40, 45].

The conditional probability tables (CPTs) for temperature, relative humidity, and CO_2 concentration nodes in the eBN shown in Fig. 10 are detailed in Tab. 16, 17, and 18, respectively. These distributions are estimated by fitting normal distributions at each time step and for each projection.

Table 16: Temperature nodes CPTs for the precise eBN of Fig. 10. Temperatures are measured in K

Node	**CPT**	
	proj	**distribution**
T_2020	ssp1	$Trunc(N(283.9; 0.85); 0, \infty)$
	ssp2	$Trunc(N(284.1; 0.85); 0, \infty)$
	ssp5	$Trunc(N(283.9; 0.85); 0, \infty)$
	proj	**distribution**
T_2030	ssp1	$Trunc(N(284.2; 0.85); 0, \infty)$
	ssp2	$Trunc(N(284.2; 0.85); 0, \infty)$
	ssp5	$Trunc(N(284.3; 1.13); 0, \infty)$

Continued on next page

Node	CPT	
T_2040	**proj**	**distribution**
	ssp1	$Trunc(N(284.2; 0.85); 0, \infty)$
	ssp2	$Trunc(N(284.6; 0.85); 0, \infty)$
	ssp5	$Trunc(N(284.9; 1.14); 0, \infty)$
T_2050	**proj**	**distribution**
	ssp1	$Trunc(N(284.5; 0.85); 0, \infty)$
	ssp2	$Trunc(N(284.8; 1.14); 0, \infty)$
	ssp5	$Trunc(N(285.4; 1.14); 0, \infty)$
T_2060	**proj**	**distribution**
	ssp1	$Trunc(N(284.7; 1.13); 0, \infty)$
	ssp2	$Trunc(N(285.1; 0.85); 0, \infty)$
	ssp5	$Trunc(N(285.9; 1.14); 0, \infty)$
T_2070	**proj**	**distribution**
	ssp1	$Trunc(N(284.7; 1.13); 0, \infty)$
	ssp2	$Trunc(N(285.2; 1.14); 0, \infty)$
	ssp5	$Trunc(N(286.5; 1.15); 0, \infty)$
T_2080	**proj**	**distribution**
	ssp1	$Trunc(N(285.0; 1.14); 0, \infty)$
	ssp2	$Trunc(N(285.4; 1.14); 0, \infty)$
	ssp5	$Trunc(N(287.4; 1.44); 0, \infty)$

Continued on next page

Node	CPT	
	proj	**distribution**
T_2090	ssp1	$Trunc(N(284.8; 1.42); 0, \infty)$
	ssp2	$Trunc(N(286.7; 1.14); 0, \infty)$
	ssp5	$Trunc(N(288.1; 1.44); 0, \infty)$
	proj	**distribution**
T_2100	ssp1	$Trunc(N(283.7; 1.42); 0, \infty)$
	ssp2	$Trunc(N(286.0; 1.14); 0, \infty)$
	ssp5	$Trunc(N(288.9; 1.45); 0, \infty)$

Table 17: RH nodes CPTs for the precise eBN of Fig. 10. RH is expressed in percentage of deviation with respect to the reference value $RH_{ref} = 0.65$

Node	CPT	
	proj	**distribution**
RH_int_2020	ssp1	$Trunc(N(9.35e^{-2}; 5.66e^{-2}); 0, 1)$
	ssp2	$Trunc(N(8.48e^{-2}; 6.42e^{-2}); 0, 1)$
	ssp5	$Trunc(N(8.19e^{-2}; 5.00e^{-2}); 0, 1)$
	proj	**distribution**
RH_int_2030	ssp1	$Trunc(N(9.52e^{-2}; 5.20e^{-2}); 0, 1)$
	ssp2	$Trunc(N(9.18e^{-2}; 5.42e^{-2}); 0, 1)$
	ssp5	$Trunc(N(1.11e^{-1}; 5.83e^{-2}); 0, 1)$

Continued on next page

Node	CPT	
	proj	**distribution**
RH_int_2040	ssp1	$Trunc(N(1.01e^{-1}; 5.67e^{-2}); 0, 1)$
	ssp2	$Trunc(N(1.12e^{-1}; 6.61e^{-2}); 0, 1)$
	ssp5	$Trunc(N(1.44e^{-1}; 7.07e^{-2}); 0, 1)$
	proj	**distribution**
RH_int_2050	ssp1	$Trunc(N(1.16e^{-1}; 6.56e^{-2}); 0, 1)$
	ssp2	$Trunc(N(1.34e^{-1}; 6.63e^{-2}); 0, 1)$
	ssp5	$Trunc(N(1.66e^{-1}; 6.73e^{-2}); 0, 1)$
	proj	**distribution**
RH_int_2060	ssp1	$Trunc(N(1.27e^{-1}; 6.63e^{-2}); 0, 1)$
	ssp2	$Trunc(N(1.50e^{-1}; 7.39e^{-2}); 0, 1)$
	ssp5	$Trunc(N(1.90e^{-1}; 7.26e^{-2}); 0, 1)$
	proj	**distribution**
RH_int_2070	ssp1	$Trunc(N(1.25e^{-1}; 6.80e^{-2}); 0, 1)$
	ssp2	$Trunc(N(1.60e^{-1}; 8.14e^{-2}); 0, 1)$
	ssp5	$Trunc(N(2.30e^{-1}; 8.92e^{-2}); 0, 1)$
	proj	**distribution**
RH_int_2080	ssp1	$Trunc(N(1.42e^{-1}; 7.54e^{-2}); 0, 1)$
	ssp2	$Trunc(N(1.71e^{-1}; 7.88e^{-2}); 0, 1)$
	ssp5	$Trunc(N(2.95e^{-1}; 1.91e^{-1}); 0, 1)$

Continued on next page

Node	CPT	
	proj	**distribution**
RH_int_2090	ssp1	$Trunc(N(1.41e^{-1}; 8.12e^{-2}); 0, 1)$
	ssp2	$Trunc(N(1.79e^{-1}; 8.25e^{-2}); 0, 1)$
	ssp5	$Trunc(N(3.28e^{-1}; 1.24e^{-1}); 0, 1)$
	proj	**distribution**
RH_int_2100	ssp1	$Trunc(N(1.34e^{-1}; 8.97e^{-2}); 0, 1)$
	ssp2	$Trunc(N(1.96e^{-1}; 8.64e^{-2}); 0, 1)$
	ssp5	$Trunc(N(3.85e^{-1}; 1.43e^{-1}); 0, 1)$

Table 18: CO_2 concentration nodes CPTs for the precise eBN of Fig. 10. CO_2 concentrations are measured in *ppm*

Node	CPT	
	proj	**distribution**
$ppm\_CO_2\_2020$	ssp1	412.5
	ssp2	412.5
	ssp5	412.5
	proj	**distribution**
$ppm\_CO_2\_2030$	ssp1	$Trunc(N(430.8; 6.89); 0)$
	ssp2	$Trunc(N(435.0; 7.83); 0)$
	ssp5	$Trunc(N(448.8; 9.87); 0)$

Continued on next page

Node	CPT	
	proj	**distribution**
$ppm\_CO_2\_2040$	ssp1	$Trunc(N(440.2; 6.89); 0)$
	ssp2	$Trunc(N(460.8; 7.37); 0)$
	ssp5	$Trunc(N(489.4; 8.80); 0)$
	proj	**distribution**
$ppm\_CO_2\_2050$	ssp1	$Trunc(N(442.7; 7.52); 0)$
	ssp2	$Trunc(N(486.5; 7.30); 0)$
	ssp5	$Trunc(N(540.5; 10.27); 0)$
	proj	**distribution**
$ppm\_CO_2\_2060$	ssp1	$Trunc(N(441.7; 4.41); 0)$
	ssp2	$Trunc(N(508.9; 8.14); 0)$
	ssp5	$Trunc(N(603.5; 9.05); 0)$
	proj	**distribution**
$ppm\_CO_2\_2070$	ssp1	$Trunc(N(437.5; 3.50); 0)$
	ssp2	$Trunc(N(524.3; 7.34); 0)$
	ssp5	$Trunc(N(677.1; 8.80); 0)$
	proj	**distribution**
$ppm\_CO_2\_2080$	ssp1	$Trunc(N(431.6; 3.88); 0)$
	ssp2	$Trunc(N(531.1; 6.37); 0)$
	ssp5	$Trunc(N(758.2; 9.86); 0)$

Continued on next page

Node	CPT	
	proj	**distribution**
$ppm\_CO_2\_2090$	ssp1	$Trunc(N(426.0; 4.26); 0)$
	ssp2	$Trunc(N(533.7; 5.34); 0)$
	ssp5	$Trunc(N(844.8; 10.13); 0)$
	proj	**distribution**
$ppm\_CO_2\_2100$	ssp1	$Trunc(N(420.9; 4.63); 0)$
	ssp2	$Trunc(N(538.4; 4.30); 0)$
	ssp5	$Trunc(N(935.9; 9.36); 0)$

B Appendix

The same data set used for Appendix A have been employed to build the intervals for each temperature node of the imprecise eBN shown in Fig. 12. Lower and upper interval bounds have been evaluated respectively as the 95% lower and upper confidence intervals.

Table 19: Temperature nodes CPTs for the imprecise eBN of Fig. 12. Temperatures are measured in K

Node	CPT		
	proj	**lb**	**ub**
T_2020	ssp1	281.8723	285.5608
	ssp2	281.6916	286.8414
	ssp5	281.5062	286.7255

Continued on next page

Node	CPT		
	proj	**lb**	**ub**
T_2030	ssp1	282.0982	287.0741
	ssp2	282.2602	286.8415
	ssp5	281.5062	286.7255
	proj	**lb**	**ub**
T_2040	ssp1	282.2752	285.7549
	ssp2	282.2368	287.6774
	ssp5	281.8712	287.1479
	proj	**lb**	**ub**
T_2050	ssp1	282.1972	286.3009
	ssp2	282.1169	286.5602
	ssp5	282.6306	287.7634
	proj	**lb**	**ub**
T_2060	ssp1	281.9507	287.6729
	ssp2	282.8809	287.8323
	ssp5	284.1444	288.1458
	proj	**lb**	**ub**
T_2070	ssp1	282.4679	286.3140
	ssp2	282.1799	287.8909
	ssp5	283.5394	289.1019

Continued on next page

Node	CPT		
	proj	**lb**	**ub**
T_2080	ssp1	282.0230	287.2399
	ssp2	283.1048	287.3655
	ssp5	284.8888	289.7104
	proj	**lb**	**ub**
T_2090	ssp1	281.3064	288.7765
	ssp2	282.5490	287.8518
	ssp5	284.3658	290.5262
	proj	**lb**	**ub**
T_2100	ssp1	281.7551	287.4349
	ssp2	283.0796	288.4324
	ssp5	285.1481	292.2743

References

[1] F. P. Glasser, J. Marchand, and E. Samson. "Durability of concrete Degradation phenomena involving detrimental chemical reactions". In: *Cement and Concrete Research* 38.2 (2008). Special Issue The 12th International Congress on the Chemistry of Cement. Montreal, Canada, July 8-13 2007, pages 226–246. ISSN: 0008-8846. DOI: https://doi.org/10.1016/j.cemconres.2007.09.015. URL: https://www.sciencedirect.com/science/article/pii/S0008884607002190.

[2] F. Qu, W. Li, W. Dong, V. W. Tam, and T. Yu. "Durability deterioration of concrete under marine environment from material to structure: A critical review". In: *Journal of Building Engineering* 35 (2021), page 102074.

[3] B. Lagerblad. "Carbon dioxide uptake during concrete life cycle - State of the art". In: *Swedish Cement and Concrete Research Institute* (2005).

[4] X. Shi, N. Xie, K. Fortune, and J. Gong. "Durability of steel reinforced concrete in chloride environments: An overview". In: *Construction and building materials* 30 (2012), pages 125–138.

[5] J. C. Walton, L. Plansky, and R. W. Smith. "Models for estimation of service life of concrete barriers in low-level radioactive waste disposal". In: (1990).

[6] T. Lindborg, M. Thorne, E. Andersson, et al. "Climate change and landscape development in post-closure safety assessment of solid radioactive waste disposal: results of an initiative of the IAEA". In: *Journal of Environmental Radioactivity* 183 (2018), pages 41–53.

[7] I. A. Papazoglou. "Mathematical Foundations of Event Trees". In: *Reliability Engineering & System Safety* 61.3 (1998), pages 169–183. ISSN: 09518320. DOI: 10.1016/S0951-8320(98)00010-6.

[8] S. Kabir. "An Overview of Fault Tree Analysis and Its Application in Model Based Dependability Analysis". In: *Expert Systems with Applications* 77 (2017), pages 114–135. ISSN: 09574174. DOI: 10.1016/j.eswa.2017.01.058.

[9] S. Mahadevan, R. Zhang, and N. Smith. "Bayesian networks for system reliability reassessment". In: *Structural Safety* 23.3 (2001), pages 231–251.

[10] H. Langseth and L. Portinale. "Bayesian Networks in Reliability". In: *Reliability Engineering & System Safety* 92.1 (2007), pages 92–108. ISSN: 09518320. DOI: 10.1016/j.ress.2005.11.037.

[11] P. G. Morato, K. G. Papakonstantinou, C. P. Andriotis, J. S. Nielsen, and P. Rigo. "Optimal inspection and maintenance planning for deteriorating structural components through dynamic Bayesian networks and Markov decision processes". In: *Structural Safety* 94 (2022), page 102140.

[12] P. Gehl and D. Dayala. "Development of Bayesian Networks for the multi-hazard fragility assessment of bridge systems". In: *Structural Safety* 60 (2016), pages 37–46.

[13] B. Barros, B. Conde, B. Riveiro, and O. Morales-Nápoles. "Gaussian Copula-based Bayesian network approach for characterizing spatial variability in aging steel bridges". In: *Structural Safety* 106 (2024), page 102403.

[14] A. Yazdani, M.-S. Shahidzadeh, and T. Takada. "Bayesian networks for disaggregation of structural reliability". In: *Structural Safety* 82 (2020), page 101892.

[15] J. Luque and D. Straub. "Risk-based optimal inspection strategies for structural systems using dynamic Bayesian networks". In: *Structural Safety* 76 (2019), pages 68–80.

[16] D. Lee and K. Kwon. “Dynamic Bayesian network model for comprehensive risk analysis of fatigue-critical structural details”. In: *Reliability Engineering & System Safety* 229 (2023), page 108834.

[17] T.-B. Tran, E. Bastidas-Arteaga, and Y. Aoues. “A Dynamic Bayesian Network framework for spatial deterioration modelling and reliability updating of timber structures subjected to decay”. In: *Engineering Structures* 209 (2020), page 110301.

[18] J. Hackl and J. Kohler. “Reliability assessment of deteriorating reinforced concrete structures by representing the coupled effect of corrosion initiation and progression by Bayesian networks”. In: *Structural Safety* 62 (2016), pages 12–23.

[19] S. A. Hosseini, F. Di Maio, and E. Zio. “A Dynamic Bayesian Network for the Performance Assessment of Nuclear Waste Repositories Undergoing Chemical Degradation due to Climate Change”. In: *2024 8th International Conference on System Reliability and Safety (ICSRS)*. IEEE. 2024, pages 385–389.

[20] H. Guo, Y. Dong, and E. Bastidas-Arteaga. “Mixed Bayesian Network for reliability assessment of RC structures subjected to environmental actions”. In: *Structural Safety* 106 (2024), page 102392.

[21] S. Russell and J. Pearl. “Computer Science Department University of California, Los Angeles, CA 90095”. In: ().

[22] D. Straub and A. Der Kiureghian. “Bayesian Network Enhanced with Structural Reliability Methods: Methodology”. In: *Journal of Engineering Mechanics* 136.10 (2010), pages 1248–1258. ISSN: 0733-9399, 1943-7889. DOI: 10.1061/(ASCE)EM.1943-7889.0000173.

[23] R. D. Shachter. "Evaluating Influence Diagrams". In: *Operations Research* 34.6 (1986), pages 871–882.

[24] M. Beer, S. Ferson, and V. Kreinovich. "Imprecise Probabilities in Engineering Analyses". In: *Mechanical Systems and Signal Processing* 37.1-2 (2013), pages 4–29. ISSN: 08883270. DOI: 10.1016/j.ymssp.2013.01.024.

[25] K. Weichselberger. "The Theory of Interval-Probability as a Unifying Concept for Uncertainty". In: *International Journal of Approximate Reasoning* 24.2-3 (2000), pages 149–170. ISSN: 0888613X. DOI: 10.1016/S0888-613X(00)00032-3.

[26] S. Ferson, V. Kreinovich, L. Ginzburg, D. Myers, and K. Sentz. "Constructing Probability Boxes and Dempster-Shafer Structures". In: (2003). DOI: 10.2172/809606.

[27] D. A. Alvarez, F. Uribe, and J. E. Hurtado. "Estimation of the lower and upper bounds on the probability of failure using subset simulation and random set theory". In: *Mechanical Systems and Signal Processing* 100 (2018), pages 782–801. ISSN: 0888-3270. DOI: https://doi.org/10.1016/j.ymssp.2017.07.040. URL: https://www.sciencedirect.com/science/article/pii/S0888327017304041.

[28] F. G. Cozman. "Credal networks". In: *Artificial Intelligence* 120.2 (2000), pages 199–233. ISSN: 0004-3702. DOI: https://doi.org/10.1016/S0004-3702(00)00029-1. URL: https://www.sciencedirect.com/science/article/pii/S0004370200000291.

[29] I. Levi. *The Enterprise of Knowledge: An Essay on Knowledge, Credal Probability, and Chance*. MIT Press, 1980.

[30] A. Perin and J. Behrensdorf. *EnhancedBayesianNetworks.jl*. 2024. DOI: https://doi.org/10.5281/zenodo.14054153. URL: https://github.com/andreaperin/EnhancedBayesianNetworks.jl.

[31] S. Talukdar, N. Banthia, and J. Grace. "Carbonation in concrete infrastructure in the context of global climate change Part 1: Experimental results and model development". In: *Cement and Concrete Composites* 34.8 (2012), pages 924–930. ISSN: 0958-9465. DOI: https://doi.org/10.1016/j.cemconcomp.2012.04.011. URL: https://www.sciencedirect.com/science/article/pii/S095894651200100X.

[32] S. Talukdar, N. Banthia, J. Grace, and S. Cohen. "Carbonation in concrete infrastructure in the context of global climate change: Part 2 Canadian urban simulations". In: *Cement and Concrete Composites* 34.8 (2012), pages 931–935. ISSN: 0958-9465. DOI: https://doi.org/10.1016/j.cemconcomp.2012.04.012. URL: https://www.sciencedirect.com/science/article/pii/S0958946512001011.

[33] M. G. Stewart, X. Wang, and M. N. Nguyen. "Climate change impact and risks of concrete infrastructure deterioration". In: *Engineering Structures* 33.4 (2011), pages 1326–1337. ISSN: 0141-0296. DOI: https://doi.org/10.1016/j.engstruct.2011.01.010. URL: https://www.sciencedirect.com/science/article/pii/S0141029611000241.

[34] E. Bastidas-Arteaga, F. Schoefs, M. G. Stewart, and X. Wang. "Influence of global warming on durability of corroding RC structures: A probabilistic approach". In: *Engineering Structures* 51 (2013), pages 259–266. ISSN: 0141-0296. DOI: https://doi.org/10.1016/j.engstruct.2013.01.006. URL: https://www.sciencedirect.com/science/article/pii/S0141029613000217.

[35] E. Bastidas-Arteaga, G. Rianna, H. Gervasio, and M. Nogal. "Multi-region lifetime assessment of reinforced concrete structures subjected to carbonation and climate change". In: *Structures* 45 (2022), pages 886–899. ISSN: 2352-0124. DOI: https://doi.org/10.1016/j.istruc.2022.09.061.

[36] I.-S. Yoon, O. Çopurolu, and K.-B. Park. "Effect of global climatic change on carbonation progress of concrete". In: *Atmospheric Environment* 41.34 (2007), pages 7274–7285. ISSN: 1352-2310. DOI: https://doi.org/10.1016/j.atmosenv.2007.05.028. URL: https://www.sciencedirect.com/science/article/pii/S135223100700461X.

[37] H. Al-Khaiat and N. Fattuhi. "Carbonation of Concrete Exposed to Hot and Arid Climate". In: *Journal of Materials in Civil Engineering - J MATER CIVIL ENG* 14 (2002). DOI: 10.1061/(ASCE)0899-1561(2002)14:2(97).

[38] B. Bary and A. Sellier. "Coupled moisturecarbon dioxidecalcium transfer model for carbonation of concrete". In: *Cement and Concrete Research* 34.10 (2004), pages 1859–1872. ISSN: 0008-8846. DOI: https://doi.org/10.1016/j.cemconres.2004.01.025. URL: https://www.sciencedirect.com/science/article/pii/S0008884604000602.

[39] J. El Hassan, P. Bressolette, A. Chateauneuf, and K. El Tawil. "Reliability-based assessment of the effect of climatic conditions on the corrosion of RC structures subject to chloride ingress". In: *Engineering Structures* 32.10 (2010), pages 3279–3287. ISSN: 0141-0296. DOI: https://doi.org/10.1016/j.engstruct.2010.07.001. URL: https://www.sciencedirect.com/science/article/pii/S0141029610002579.

[40] Copernicus Climate Change Service. *CMIP6 predictions underpinning the C3S decadal prediction prototypes*. 2021.

[41] D. M. Francesco, F. Matteo, G. Carlo, P. Federico, and Z. Enrico. "Time-dependent reliability analysis of the reactor building of a nuclear power plant for accounting of its aging and degradation". In: *Reliability Engineering & System Safety* 205 (2021), page 107173. ISSN: 0951-8320. DOI: https://doi.org/10.1016/j.ress.2020.107173. URL: https://www.sciencedirect.com/science/article/pii/S0951832020306748.

[42] I. Sobol. "Global sensitivity indices for nonlinear mathematical models and their Monte Carlo estimates". In: *Mathematics and Computers in Simulation* 55.1 (2001). The Second IMACS Seminar on Monte Carlo Methods, pages 271–280. ISSN: 0378-4754. DOI: https://doi.org/10.1016/S0378-4754(00)00270-6. URL: https://www.sciencedirect.com/science/article/pii/S0378475400002706.

[43] P. Wei, J. Song, S. Bi, M. Broggi, M. Beer, Z. Lu, and Z. Yue. "Non-Intrusive Stochastic Analysis with Parameterized Imprecise Probability Models: II. Reliability and Rare Events Analysis". In: *Mechanical Systems and Signal Processing* 126 (2019), pages 227–247. ISSN: 0888-3270. DOI: 10.1016/j.ymssp.2019.02.015.

[44] F. Hong, P. Wei, J. Fu, and M. Beer. "A Sequential Sampling-Based Bayesian Numerical Method for Reliability-Based Design Optimization". In: *Reliability Engineering & System Safety* 244 (2024), page 109939. ISSN: 09518320. DOI: 10.1016/j.ress.2024.109939.

[45] B. C. O'Neill, C. Tebaldi, D. P. van Vuuren, et al. "The Scenario Model Intercomparison Project (ScenarioMIP) for CMIP6". In: *Geoscientific Model Development* 9.9 (2016), pages 3461–3482. DOI: 10.5194/gmd-9-3461-2016.